# Large-Area Synthesis of Highly Crystalline WSe$_2$ Monolayers and Device Applications

Jing-Kai Huang,[†] Jiang Pu,[‡] Chang-Lung Hsu,[†] Ming-Hui Chiu,[†] Zhen-Yu Juang,[†] Yung-Huang Chang,[†] Wen-Hao Chang,[§] Yoshihiro Iwasa,[⊥] Taishi Takenobu,[‡,*] and Lain-Jong Li[†,∥,*]

[†]Institute of Atomic and Molecular Sciences, Academia Sinica, Taipei 106, Taiwan, [‡]Department of Applied Physics, Waseda University, Tokyo 169-8555, Japan, [§]Department of Electrophysics, National Chiao Tung University, Hsinchu 300, Taiwan, [⊥]Quantum-Phase Electronics Center and Department of Applied Physics, School of Engineering, The University of Tokyo, Hongo, Bunkyo, Tokyo 113-8654, Japan, and [∥]Department of Medical Research, China Medical University Hospital, Taichung, Taiwan

ABSTRACT The monolayer transition metal dichalcogenides have recently attracted much attention owing to their potential in valleytronics, flexible and low-power electronics, and optoelectronic devices. Recent reports have demonstrated the growth of large-size two-dimensional MoS$_2$ layers by the sulfurization of molybdenum oxides. However, the growth of a transition metal selenide monolayer has still been a challenge. Here we report that the introduction of hydrogen in the reaction chamber helps to activate the selenization of WO$_3$, where large-size WSe$_2$ monolayer flakes or thin films can be successfully grown. The top-gated field-effect transistors based on WSe$_2$ monolayers using ionic gels as the dielectrics exhibit ambipolar characteristics, where the hole and electron mobility values are up to 90 and 7 cm^2/Vs, respectively. These films can be transferred onto arbitrary substrates, which may inspire research efforts to explore their properties and applications. The resistor-loaded inverter based on a WSe$_2$ film, with a gain of ∼13, further demonstrates its applicability for logic-circuit integrations.
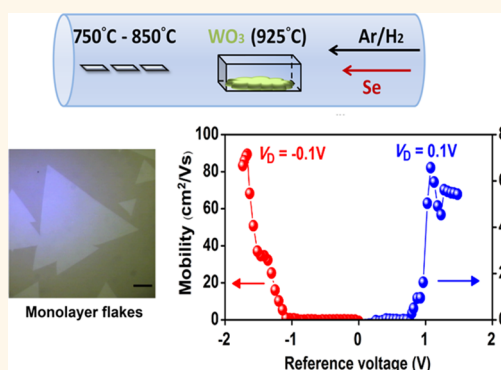
Monolayer flakes

Transition metal dichalcogenides (TMDs) have attracted much attention due to their two-dimensional (2-d) layer structure, where a sheet of metal atoms is sandwiched between two sheets of chalcogens by covalent interaction. Depending on the selection of the metal, these layered materials may exhibit superconducting, metallic, or semiconducting properties.[1−4] Moreover, the electronic structures of the semiconducting TMDs such as molybdenum disulfide (MoS$_2$), tungsten disulfide (WS$_2$), and tungsten diselenide (WSe$_2$) vary with their thickness. For example, the optical transition of MoS$_2$ transforms from the indirect gap in a bulk form to the direct gap when it is a monolayer sheet.[5−13] These monolayer TMD films are highly bendable and thus promising for flexible electronics.[14] Another important feature of the 2-d TMD films is that their properties are

sensitive to the electrostatic interaction or a gate voltage.[15,16] Recently, it has been demonstrated that the field-effect transistors fabricated with the MoS$_2$ thin layers exhibit an excellent on/off current ratio and a reasonably good carrier mobility.[17,18] So far, most of the transistors based on either exfoliated or synthetic MoS$_2$ layers show an n-type behavior. Very recent reports have demonstrated the formation of MoS$_2$ p−n junction devices by using electric double-layer gating[19,20] or creating p-doped MoS$_2$ by efficient plasma treatment.[21,22] At the same time, the research for an intrinsically p-type TMD monolayer becomes urgent for realizing complementary digital logic applications. Actually, the p-type transistor behaviors have been observed in bulk and mechanically exfoliated monolayer or few-layer WSe$_2$ flakes.[23,24] Recent studies have made significant advances in

understanding the role of contact metals on the electrical characteristics of the transistors made from exfoliated WSe_2 flakes.[23,25] However, the large-scale device applications still rely on the breakthrough in the growth of large-size WSe_2 thin layers. Early approaches including the thermal decomposition of WSe_3,[26] direct heating of the mixture of W and Se elements,[27−31] vapor transport growth of WSe_2,[32] and the reaction of WO_3 fine powders with H_2Se[33] or Se[34] have led to successful growth of WSe_2 crystals or fullerene-like particles but not atomically thin layers. Recent progress on the growth of monolayer MoS_2 by the sulfurization of molybdenum oxides[35−38] in vapor phases, where the formation of MoS_2 atomically thin layers is based on the reaction of MoO_3 and sulfur vapors, has shed light on the large-area preparation of other TMD monolayer materials. In this contribution, we report that the introduction of hydrogen in the reaction environment is necessary for the growth of a highly crystalline WSe_2 monolayer using the vapor phase reaction of WO_3 and Se. The field-effect transistors based on the as-grown WSe_2 monolayers exhibit ambipolar behaviors with high mobility values in both p- and n-channels.

RESULTS AND DISCUSSION

Figure 1a schematically illustrates our experimental setup for growing thin WSe_2 layers by the selenization of WO_3 powders in a hot-wall chemical vapor deposition (CVD) chamber. The morphology of the WSe_2 grown on the sapphire substrates varies with the substrate temperatures. The optical micrograph (OM) in Figure 1b shows that the WSe_2 grown at 850 °C exhibits a triangular shape, and the lateral size of each triangle is larger than 10 μm and up to 50 μm, where the lateral size may have a limit due to the high energy caused by the lattice mismatch between the WSe_2 and sapphire substrates. Meanwhile, the sparsely distributed triangles indicate that the nucleation density of the WSe_2 is low. Figure 1c is the OM image for the WSe_2 grown at a lower temperature at 750 °C, where many small WSe_2 domains merge to form a continuous film. The domain size of the WSe_2 formed at 750 °C is around several to 5 μm, as shown in the SEM image in Supporting Information Figure S1 for the nearly merged WSe_2 grown at 750 °C. These observations are reasonable since a lower growth temperature typically results in a higher nucleation density. It is noteworthy that the orientation of these small WSe_2 triangles grown at 750 °C aligns to a certain direction, implying the epitaxial growth feature of the process. Figure 1d shows the atomic force microscopic (AFM) image for the WSe_2 triangle grown at 850 °C, where the thickness of 0.73 nm of the film is in agreement with the reported thickness for mechanically exfoliated WSe_2 monolayers.[23,25] The AFM image and cross-section profile in Figure S2 obtained for the WSe_2 film
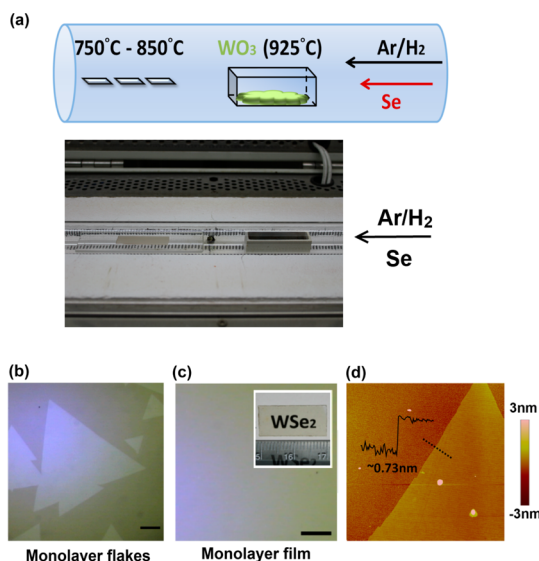
Figure 1. (a) Schematic illustration for the growth of WSe_2 layers on sapphire substrates by the reaction of WO_3 and Se powders in a CVD furnace. A photo of the setup is also shown. (b,c) Optical microscopy images of the WSe_2 monolayer flakes and monolayer film grown at 850 and 750 °C, respectively. Scale bar is 10 μm in length. The inset in (c) shows the photograph of a uniform monolayer film grown on a double side polished sapphire substrate. (d) AFM image of a WSe_2 monolayer flake grown at 850 °C on a sapphire substrate.

grown at 750 °C also prove that the continuous film is a monolayer. For the WSe_2 flakes grown at 850 °C, most of the flakes are characterized as monolayers, but we still occasionally observe the growth of second layer WSe_2 on top of some large monolayer flakes, as shown in the OM in Figure 2a. The AFM cross-sectional height profile for the sample shown in Figure S3 confirms that the additional layer on top is a monolayer. Note that we have also performed the WSe_2 growth on SiO_2 substrates, but the same growth method preferentially leads to particle-like structures, not a two-dimensional film. It is likely that the growth of WSe_2 has strong surface sensitivity.

Raman spectra for the monolayer and bilayer WSe_2 excited by a 473 nm laser are shown in Figure 2b, where the two characteristic peaks for monolayer WSe_2 at 248 cm^{-1}, assigned to E^1_{2g} mode, and 259 cm^{-1}, assigned to A_{1g} mode, are observed.[39,40] For the bilayer WSe_2, the A_{1g} mode slightly left shifts compared with that of monolayer WSe_2, which is consistent with the observation in ref 39. Other high-energy bands at 358.5 and 373.5 cm^{-1}, attributed to the $2E_{1g}$ and $A_{1g}+LA$ modes, are also identified.[41−43] Most importantly, the Raman band at 308 cm^{-1}, which has been reported to be related to the interlayer interaction,[44] is not observed in our WSe_2 monolayer. Instead, this characteristic peak exhibits in the Raman spectrum for our bilayer WSe_2, consistent with the results in ref 39. Figure 2c displays the optical absorption spectrum for the monolayer WSe_2 film. The excitonic absorption
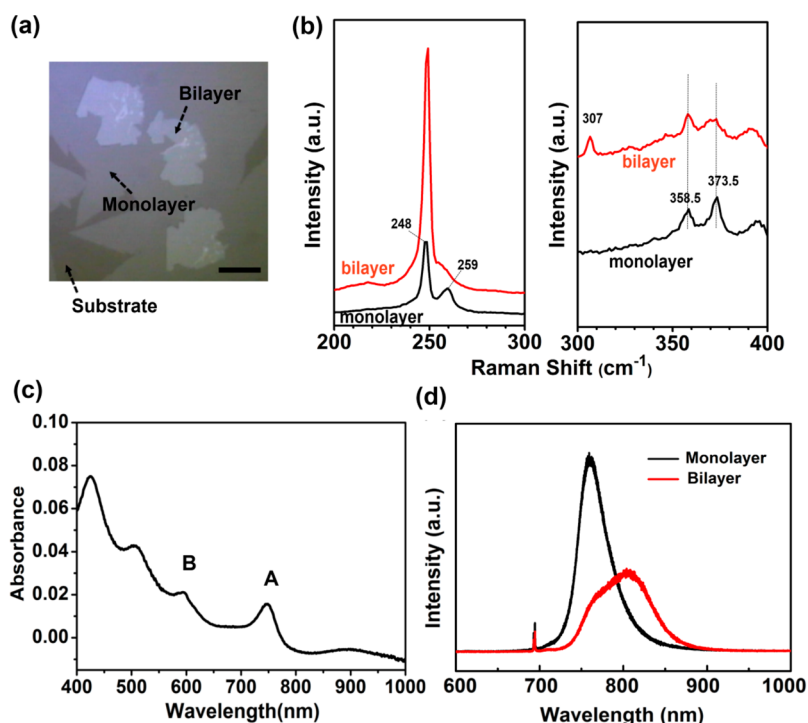
Figure 2. (a) Optical microscopic image of the second layer WSe$_2$ on top of some large monolayer flakes. Scale bar is 10 μm in length. (b) Raman spectra for the monolayer and bilayer WSe$_2$, obtained in a confocal Raman spectrometer excited by a 473 nm laser. (c) Optical absorption spectrum for the continuous WSe$_2$ film. (d) Photoluminescence spectra for the CVD WSe$_2$ monolayer and bilayer, obtained in a microscopic PL system (excitation wavelength 532 nm).

peaks A and B, arising from direct gap transitions at the K point, are identified at around 750 and 595 nm respectively, agreeing well with previous reports.[45−47] Figure 2d compares the PL spectra (excited by a 532 nm laser) of monolayer and bilayer WSe$_2$ areas. The PL spectrum for the monolayer WSe$_2$ flake exhibits a strong emission at ~760 nm corresponding to the A excitonic absorption, whereas the emission intensity of the same peak is much lower in the bilayer WSe$_2$. Moreover, in addition to the A exciton peak, another peak at a longer wavelength (~806 nm), attributed to the indirect band gap emission, is observed for the bilayer WSe$_2$. It is noted that the indirect gap emission is absent in a monolayer, and the distinctly strong emission from a monolayer is in good agreement with the recent report.[48−50] All of these PL observations further confirm the layer number assignment for our CVD WSe$_2$ samples.

X-ray photoemission spectroscopy (XPS) was used to measure the binding energies of the W and Se in our CVD WSe$_2$ monolayer film. Figure 3a,b shows the binding energy profiles for W 4f and Se 1s. The peaks at 32.8 and 35.0 eV are attributed to the doublet W 4f$_{7/2}$ and W 4f$_{5/2}$ binding energies, respectively. The peaks at 55 and 55.9 eV correspond to the Se 3d$_{5/2}$ and Se 3d binding energies. All of these results are consistent with the reported values for the WSe$_2$ crystal.[51,52] It is noted that Figure 3a does show the presence of weak peaks for WO$_3$ at 35.8 and 38.0 eV (the doublet W 4f$_{7/2}$ and W 4f$_{5/2}$ for WO$_3$, respectively). This is caused by the

occasionally deposited WO$_3$ particles on the surface of WSe$_2$. The domain edge of the WSe$_2$ may also contribute to the WO$_3$ signals. Figure S4 displays the SEM image showing the formation of some WO$_3$ particles during the growth of WSe$_2$ film. Nevertheless, the ratio between W and Se elements obtained from the integrated peak area after excluding the WO$_3$ part is 1:1.988, suggesting that our CVD WSe$_2$ exhibits reasonably good stoichiometry.

The tunneling electron microscopy (TEM) image in Figure 3c shows the periodic atom arrangement of the WSe$_2$ monolayer, demonstrating that the CVD WSe$_2$ film is highly crystalline. The inset shows the selected area electron diffraction (SAED) pattern taken with an aperture size of ~160 nm for the sample. Figure 3d is the magnified TEM image for the area squared by dashed lines in Figure 3c, where the high-resolution TEM image and the corresponding SAED pattern with [001] zone axis (inset of Figure 3c) reveal the hexagonal lattice structure with the lattice spacing of 0.38 and 0.33 nm assigned to the (100) and (110) planes.[53]

It is noteworthy pointing out that, for the synthesis of a MoS$_2$ monolayer using the same method,[35] the sulfurization of MoO$_3$ is typically performed at 650 °C in an Ar environment, where the chemical reaction is described as

$$2MoO_3 + 7S \rightarrow 2MoS_2 + 3SO_2 \qquad (1)$$
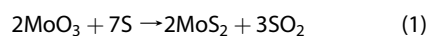
The introduction of a reducer such as hydrogen in the reaction atmosphere is not necessary. However, the
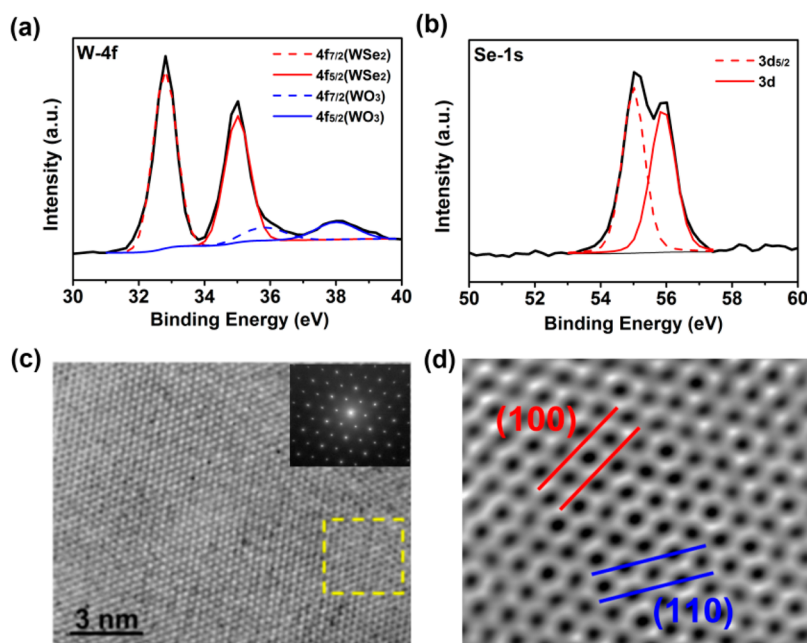
Figure 3. (a,b) XPS spectra of the WSe$_2$ monolayer film, where the (a) W 4f and (b) Se 1s binding energies are identified. The two peaks at 32.8 and 35.0 eV are attributed to the doublet W 4f$_{7/2}$ and W 4f$_{5/2}$. Note that the peaks at 35.8 and 38.0 eV are attributed to the doublet W 4f$_{7/2}$ and W 4f$_{5/2}$ for WO$_3$. The binding energy at 55 and 55.9 eV can be assigned to the Se 3d$_{5/2}$ and Se 3d binding energies, respectively. (c) High-resolution TEM image of WSe$_2$ monolayer with an inset showing its SAED pattern. (d) Enlarged TEM image for the marked area in (c).

chemical reactivity of Se is much lower than that of S, and thus a strong reducer like hydrogen is required in the selenization reaction of WO$_3$. In our experiments, we also observe that no WSe$_2$ is obtained if no hydrogen gas is introduced in the chamber. The thermodynamic calculations have also corroborated that the selenization reaction of WO$_3$ is only possible with the presence of hydrogen.[34] The chemical reaction occurring during the selenization of WO$_3$ is as follows:

$$WO_3 + 3Se + H_2 \rightarrow WSe_2 + H_2O + SeO_2 \qquad (2)$$

Note that if the hydrogen ratio is too high, the reduction of WO$_3$ to W metal proceeds very efficiently. The WO$_3$ evaporation rate thus becomes relatively slow, which does not favor the formation of WSe$_2$. The Ar/H$_2$ ratio of 4:1 was an optimized parameter based on our experiments and above rationale.

To evaluate the quality of the synthetic WSe$_2$ monolayer, we measured the electrical properties of the electric double-layer transistors (EDLT) based on the as-grown WSe$_2$ monolayer film on sapphire substrates. EDLT is known as a good method to determine the mobility at a high carrier concentration, which is not easily accessed by solid insulator gating. Figure 4a shows the OM image for the EDLT device top view, where the channel width and length are 668 and 1225 μm, respectively. Figure 4b shows the output characteristics for both the p- and n-channels at various reference voltages (V_R) as specified in graphs. Note that the V_R is the measured voltage between the electrolytes and WSe$_2$, that is, the voltage for the

electric double layer on WSe$_2$ surfaces, and it is normally smaller than the applied gate voltage on the top Pt metal since the gate voltage is partially consumed by the electric double layer on the gate electrode. The correlation between the applied gate voltage and the reference voltage is shown in Figure S5. It is observed that the source–drain current exhibits an obvious saturation regime for all curves. To obtain the capacitance of the WSe$_2$/ion gel surface, the source and drain electrodes are short-circuited, and two terminal measurements across the source/drain and top-gate electrodes are carried out. The frequency range is set to 10^{-3}–10^5 Hz. As shown in Figure S6, the phase angle becomes approximately $-90°$, and the estimated capacitance is almost constant when the frequency is <100 Hz. Especially, for dc voltage dependence of ion gel capacitance, the frequency is set to 10 Hz with an ac voltage amplitude of 5 mV, and dc voltage is applied from -3.2 to 3.4 V. The measurement result for the specific capacitance at various reference voltages is shown in Figure 4c. The dependence of the capacitance on V_R reveals a step-function-like profile for both p- and n-channels, which is reasonably explained by competition of geometrical and quantum capacitances. Owing to the high ionic concentration of the ion gel and the large specific surface area of the 2-d TMD film, the measured capacitance consists of two major contributions: the quantum capacitance and the interfacial capacitance arising from the electric double layer formed by ions at the WSe$_2$–ion gel interface, which can be modeled as two capacitors in series.[54]
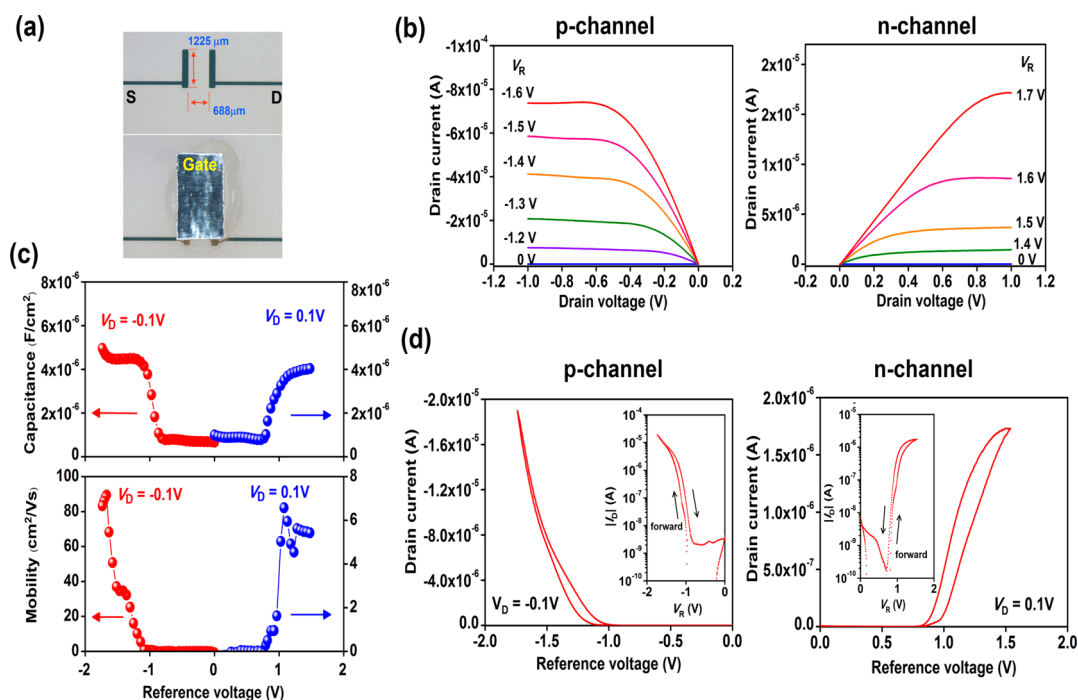
Figure 4. (a) Optical micrograph of the top view for the WSe$_2$ EDLT device, where the top and bottom photos were taken before and after the ion gel/top gate deposition. (b) Output characteristics of the WSe$_2$ EDLT device. (c) Specific capacitance and carrier mobility values measured at various reference voltages. The drain current level was maintained at ± 0.1 V, which was in the linear regime. (d) Typical transfer curves for the EDLT device, where the inset in each graph shows the transfer curve plotted in a log scale.

The measured capacitance is dominated by the quantum capacitance when the V_R is inside the E_g of WSe$_2$, whereas the capacitance is governed by the geometrical capacitance when the V_R is outside the E_g. Note that the effect of in-gap states is negligible due to the huge geometrical capacitance of the ion gel. Based on this argument, the E_g of WSe$_2$ can be estimated to be the difference between the rising onset points in p-channel (-0.82 V) and n-channel (0.79 V), that is, $\sim$1.61 V, where the number approximately agrees with the energy band gap ($E_g \sim 1.6$ eV) of WSe$_2$ monolayer. Moreover, the field-effect mobility was calculated by the standard formula for the linear region, $\mu = (L/WC_iV_D) \times (\Delta I_D/\Delta V_R)$, where μ is the field-effect mobility, W is the channel width, V_D is the drain voltage, C_i is the measured specific capacitance of the ion gel, L is the channel length, and I_D is the drain current.

Figure 4d displays the p- and n-transfer curves (drain current vs V_R) of a WSe$_2$ monolayer EDLT at the applied drain voltage $V_D = -0.1$ and 0.1 V, respectively. Consistent with the report for thick WSe$_2$ crystals by Podzorov et al.,[24] we clearly observe an ambipolar transport behavior with ohmic-like current−voltage characteristics. The inset in each graph replots the drain current from a linear to a log scale, and the on−off current ratio is as high as 10^5 and 10^4 for p- and n-channels. The reference voltage dependence of carrier mobilities from capacitance measurements in Figure 4c also shows a step-like profile. The highest carrier mobility is 90 cm^2/Vs for the hole transport and

7 cm^2/Vs for the electron transport. It is noted that Figure S7 provides the transfer curves, mobility, and capacitance dependences on V_R performed in the saturation regime, and these results are consistent with those measured in the linear regime. Figure S8 shows the electrical characteristics for the two devices fabricated on the same WSe$_2$ film (spaced by 1 cm). The devices with three channel lengths (7, 10, and 6 μm) have also been fabricated. Table S1 lists all the characteristics including V_{th}, S, mobility, and I_{on}/I_{off} for the eight devices we prepared. The electrical results for all devices are quite consistent. Figure 4c explores that the Ni source and drain metals form a midgap Schottky barrier with WSe$_2$ film. The higher hole mobility of the device is mainly because the Ni S/D electrodes are more accommodating at the p-channel Fermi level.

To examine the logic operation capability, we have fabricated a simple resistor-loaded inverter by connecting WSe$_2$ monolayer EDLTs in series with 500 kΩ commercial resistors. The circuit diagram and input (V_{in})−output (V_{out}) voltage characteristics are presented in Figure 5a. Using the p-type operation of a WSe$_2$ monolayer EDLT with the mobility of 50 cm^2/Vs and the on−off current ratio of 10^6, ideal inverter actions were observed. The output voltage switched near $V_{in} = 1$ V, and the inverter was completely switched within 0.5 V of the V_{in} variation. The voltage gain, defined as the negative of dV_{out}/dV_{in}, plotted in Figure 5b was approximately 13. For the successful implementation of digital logics in electronic circuits
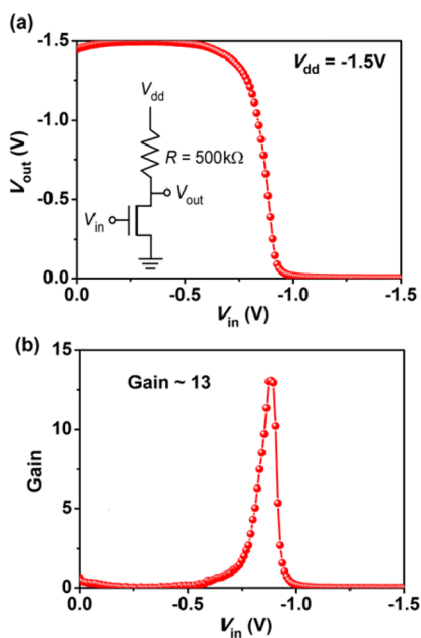
Figure 5. (a) Circuit diagram and input (V_{in})–output (V_{out}) voltage characteristics, and (b) voltage gain (defined as the negative of dV_{out}/dV_{in}) of the resistor-loaded WSe$_2$ inverter.

based on any new nanomaterial, a voltage gain more than 1 is needed so that the output of one inverter

could drive the input of the next inverter in the cascade. Therefore, our inverter is readily applicable for the integration in arrays of logic gates.

CONCLUSIONS

In conclusion, we have synthesized highly crystalline and large-area WSe$_2$ monolayers by the gas phase reaction of WO$_3$ and Se powders in a hot-wall CVD chamber. It is concluded that the hydrogen gas plays an important role to activate the reaction. Triangle and single-crystalline WSe$_2$ monolayer flakes can be grown at 850 °C, whereas a lower temperature 750 °C results in a continuous and polycrystalline monolayer film. The WSe$_2$ transistors based on ion gel gating exhibit an ambipolar behavior with high carrier mobility values. The proof-of-concept WSe$_2$-based inverter exhibits a high gain of ~13, demonstrating that synthetic WSe$_2$ layers can serve as a building block for future logic circuits based on 2-d materials. The crystalline sapphire is a good template for WSe$_2$ growth. However, the sapphire substrate is not cheap; hence, the growth of 2-d materials on other substrates is urgently needed. Actually, the growth method reported here should also be applicable to other substrates such as quartz and SiO$_2$/Si, while more efforts are required to create good nucleation environments for WSe$_2$.

METHODS

Growth of WSe$_2$ Layers. The WO$_3$ powders (0.3 g) were placed in a ceramic boat located in the heating zone center of the furnace. The Se powders were placed in a separate ceramic boat at the upper stream side maintained at 270 °C during the reaction. The sapphire substrates for growing WSe$_2$ were put at the downstream side, where the Se and WO$_3$ vapors were brought to the targeting sapphire substrates by an Ar/H$_2$ flowing gas (Ar = 80 sccm, H$_2$ = 20 sccm, chamber pressure = 1 Torr). The center heating zone was heated to 925 °C at a ramping rate of 25 °C/min. Note that the temperature of the sapphire substrates was at ~750 to 850 °C when the center heating zone reaches 925 °C. After reaching 925 °C, the heating zone was kept for 15 min and the furnace was then naturally cooled to room temperature.

Fabrication of EDLT Devices. For the EDLT source and drain electrodes, Au contacts with Ni adhesion layers (70 nm/2 nm) were thermally deposited onto the surface of the WSe$_2$ films. The ion gels, a mixture of a triblock copolymer, poly(styrene-*block*-methyl methacrylate-*block*-styrene) (PS-PMMA-PS; M_{PS} = 4.3 kg/mol, M_{PMMA} = 12.5 kg/mol, M_w = 21.1 kg/mol), and an ionic liquid, 1-ethyl-3-methylimidazolium bis(trifluoromethylsulfonyl)imide ([EMIM][TFSI]) in an ethyl propionate solution, are used as the top gate dielectrics.[14] Note that the weight ratio of the polymer, ionic liquid, and solvent was maintained at 0.7:9.3:20. This solution was drop-casted onto and covered the surfaces of WSe$_2$ film and the source and drain electrodes. The transistor channel was then covered with a thin Pt foil (thickness of 0.03 mm) to form the top-gate electrode. Finally, a thin gold wire was inserted into the gel films, between the channel and top gate metal, as the reference electrode.

Characterizations. The AFM images were performed in a Veeco Dimension-Icon system. Raman spectra were collected in a confocal Raman system (NT-MDT). The wavelength of laser is 473 nm (2.63 eV); the spot size of the laser beam is ~0.5 μm, and the spectral resolution is 3 cm^{-1} (obtained with a

600 grooves/mm grating). The Si peak at 520 cm^{-1} was used as a reference for wavenumber calibration. The WSe$_2$ films were transferred onto a copper grid for TEM observation. HRTEM imaging was performed on JEOL-2100F FEG-TEM operated at 100 kV. Chemical configurations were determined by X-ray photoelectron spectroscopy (XPS, Phi V6000). XPS measurements were performed with an Mg Kα X-ray source on the samples. The energy calibrations were made against the C 1s peak to eliminate the charging of the sample during analysis. All electrical characterizations were performed using a semiconductor parameter analyzer (Agilent E5270) in a shield probe station inside a N$_2$-filled glovebox. We perform the impedance measurements using a frequency response analyzer (a Solartron 1252A frequency response analyzer with a Solartron 1296 dielectric interface controlled by ZPlot and ZView software).

Conflict of Interest: The authors declare no competing financial interest.

Supporting Information Available: Figures S1–S8 and Table S1 are included. This material is available free of charge *via* the Internet at http://pubs.acs.org.

REFERENCES AND NOTES

1. Chhowalla, M.; Shin, H. S.; Eda, G.; Li, L.-J.; Loh, K. P.; Loh Zhang, H. The Chemistry of Two-Dimensional Layered Transition Metal Dichalcogenide Nanosheets. *Nat. Chem.* **2013**, *5*, 263–275.

2. Ataca, C.; Sahin, H.; Ciraci, S. Stable, Single-Layer MX_2 Transition-Metal Oxides and Dichalcogenides in a Honeycomb-like Structure. *J. Phys. Chem. C* **2012**, *116*, 8983–8999.

3. Huang, X.; Zeng, Z.; Zhang, H. Metal Dichalcogenide Nanosheets: Preparation, Properties and Applications. *Chem. Soc. Rev.* **2013**, *42*, 1934.

4. Kashid, R. V.; Late, D. J.; Chou, S. S.; Huang, Y.-K.; De, M.; Joag, D. S.; More, M. A.; Dravid, V. P. Enhanced Field-Emission Behavior of Layered MoS_2 Sheets. *Small* **2013**, *9*, 2730–2734.

5. Splendiani, A.; Sun, L.; Zhang, Y.; Li, T.; Kim, J.; Chim, C.-Y.; Galli, G.; Wang, F. Emerging Photoluminescence in Monolayer MoS_2. *Nano Lett.* **2010**, *10*, 1271–1275.

6. Aharon, E.; Albo, A.; Kalina, M.; Frey, G. L. Stable Blue Emission from a Polyfluorene/Layered-Compound Guest/Host Nanocomposite. *Adv. Funct. Mater.* **2006**, *16*, 980–986.

7. Mak, K. F.; Lee, C.; Hone, J.; Shan, J.; Heinz, T. F. Atomically Thin MoS_2: A New Direct-Gap Semiconductor. *Phys. Rev. Lett.* **2010**, *105*, 136805-1-4.

8. Lee, C.; Yan, H.; Brus, L. E.; Heinz, T. F.; Hone, J.; Ryu, S. Anomalous Lattice Vibrations of Single- and Few-Layer MoS_2. *ACS Nano* **2010**, *4*, 2695–2700.

9. Molina-Sánchez, A.; Wirtz, L. Phonons in Single-Layer and Few-Layer MoS_2 and WS_2. *Phys. Rev. B* **2011**, *84*, 155413-1-8.

10. Korn, T.; Heydrich, S.; Hirmer, M.; Schmutzler, J.; Schüller, C. Low-Temperature Photocarrier Dynamics in Monolayer MoS_2. *Appl. Phys. Lett.* **2011**, *99*, 102109-1-3.

11. Ghatak, S.; Pal, A. N.; Ghosh, A. Nature of Electronic States in Atomically Thin MoS_2 Field-Effect Transistors. *ACS Nano* **2011**, *5*, 7707–7712.

12. Eda, G.; Yamaguchi, H.; Voiry, D.; Fujita, T.; Chen, M.; Chhowalla, M. Photoluminescence from Chemically Exfoliated MoS_2. *Nano Lett.* **2011**, *11*, 5111–5116.

13. Zeng, H.; Dai, J.; Yao, W.; Xiao, D.; Cui, X. Valley Polarization in MoS_2 Monolayers by Optical Pumping. *Nat. Nanotechnol.* **2012**, *7*, 490–493.

14. Pu, J.; Yomogida, Y.; Liu, K.-K.; Li, L.-J.; Iwasa, Y.; Takenobu, T. Highly Flexible MoS_2 Thin-Film Transistors with Ion Gel Dielectrics. *Nano Lett.* **2012**, *12*, 4013–4017.

15. Mak, K. F.; He, K.; Lee, C.; Lee, G. H.; Hone, J.; Heinz, T. F.; Shan, J. Tightly Bound Trions in Monolayer MoS_2. *Nat. Mater.* **2013**, *12*, 207–211.

16. Zhang, W.; Chuu, C.-P.; Huang, J.-K.; Chen, C.-H.; Tsai, M.-L.; Chang, Y.-H.; Liang, C.-T.; He, J.-H.; Chou, M.-Y.; Li, L.-J. Ultrahigh-Gain Phototransistors Based on Graphene-MoS_2 Heterostructures. *arXiv:1302.1230*, **2013**, submitted on 5 Feb 2013.

17. Radisavljevic, B.; Radenovic, A.; Brivio, J.; Giacometti, V.; Kis, A. Single-Layer MoS_2 Transistors. *Nat. Nanotechnol.* **2011**, *6*, 147–150.

18. Liu, H.; Neal, A. T.; Ye, P. D. Channel Length Scaling of MoS_2 MOSFETs. *ACS Nano* **2012**, *6*, 8563–8569.

19. Zhang, Y. J.; Ye, J. Y.; Yomogida, Y.; Takenobu, T.; Iwasa, Y. Formation of a Stable p–n Junction in a Liquid-Gated MoS_2 Ambipolar Transistor. *Nano Lett.* **2013**, *13*, 3023–3028.

20. Zhang, Y. J.; Ye, J. T.; Matsuhashi, Y.; Iwasa, Y. Ambipolar MoS_2 Thin Flake Transistors. *Nano Lett.* **2012**, *12*, 1136–1140.

21. Nam, H.; Wi, S.; Rokni, H.; Chen, M.; Priessnitz, G.; Lu, W.; Liang, X. MoS_2 Transistors Fabricated *via* Plasma-Assisted Nanoprinting of Few-Layer MoS_2 Flakes into Large-Area Arrays. *ACS Nano* **2013**, *7*, 5870–5881.

22. Chen, M.; Nam, H.; Wi, S.; Ji, L.; Ren, X.; Bian, L.; Lu, S.; Liang, X. Stable Few-Layer MoS_2 Rectifying Diodes Formed by Plasma-Assisted Doping. *Appl. Phys. Lett.* **2013**, *103*, 142110-1-3.

23. Fang, H.; Chuang, S.; Chang, T. C.; Takei, K.; Takahashi, T.; Javey, A. High-Performance Single Layered WSe_2 p-FETs with Chemically Doped Contacts. *Nano Lett.* **2012**, *12*, 3788–3792.

24. Podzorov, V.; Gershenson, M. E.; Kloc, Ch.; Zeis, R.; Bucher, E. High-Mobility Field-Effect Transistors Based on Transition Metal Dichalcogenides. *Appl. Phys. Lett.* **2004**, *84*, 3301–3303.

25. Liu, W.; Kang, J.; Sarkar, D.; Khatami, Y.; Jena, D.; Banerjee, K. Role of Metal Contacts in Designing High-Performance Monolayer n-Type WSe_2 Field Effect Transistors. *Nano Lett.* **2013**, *13*, 1983–1990.

26. Glemser, O.; Sauer, H.; König, P. Uber Wolframsulfide und Wolframselenide. *Z. Anorg. Chem.* **1948**, *257*, 241–246.

27. Schäfer, H.; Wehmeier, F.; Trenkel, M. Chemischer Transport mit Schwefel als Transportmittel. *J. Less-Common Met.* **1968**, *16*, 290–291.

28. Al-Hilli, A. A.; Evans, B. L. The Preparation and Properties of Transition Metal Dichalcogenide Single Crystals. *J. Cryst. Growth* **1972**, *15*, 93–101.

29. Brixner, L. H. Preparation and Properties of the Single Crystalline AB_2-Type Selenides and Tellurides of Niobium, Tantalum, Molybdenum and Tungsten. *J. Inorg. Nucl. Chem.* **1962**, *24*, 257–263.

30. Brixner, L. H. X-ray Study and Thermoelectric Properties of the $W_x Ta_{1-x} Se_2$ System. *J. Electrochem. Soc.* **1963**, *110*, 289–293.

31. Hicks, W. T. Semiconducting Behavior of Substituted Tungsten Diselenide and Its Analogues. *J. Electrochem. Soc.* **1964**, *111*, 1058–1065.

32. Merzhanov, A. G. Properties of WSe_2 Produced by Self-Propagating High-Temperature Synthesis. *Izv. Akad. Nauk SSSR, Neorg. Mater.* **1977**, *13*, 811–814.

33. Obolonchik, V. A.; Prokoshink, L. M. Synthesis of Selenides of the Transition Metals by the Interaction of the Oxides with Hydrogen Selenide. *Zh. Prikl. Khim. Leningrad* **1971**, *44*, 2160.

34. Tsirlina, T.; Feldman, Y.; Homyonfer, M.; Sloan, J.; Hutchison, J. L.; Tenne, R. Synthesis and Characterization of Inorganic Fullerene-like WSe_2 Material. *Fullerene Sci. Technol.* **1998**, *6*, 157–165.

35. Lee, Y. H.; Zhang, X. Q.; Zhang, W.; Chang, M. T.; Lin, C. T.; Chang, K. D.; Yu, Y.-C.; Wang, T. W.; Chang, C.-S.; Li, L. J.; *et al.* Synthesis of Large-Area MoS_2 Atomic Layers with Chemical Vapor Deposition. *Adv. Mater.* **2012**, *24*, 2320–2325.

36. Lee, Y.-H.; Yu, L.; Wang, H.; Fang, W.; Ling, X.; Shi, Y.; Lin, C.-T.; Huang, J.-K.; Chang, M.-T.; Chang, C.-S.; *et al.* Synthesis and Transfer of Single Layer Transition Metal Disulfides on Diverse Surfaces. *Nano Lett.* **2013**, *13*, 1852–1857.

37. Lin, Y.-C.; Zhang, W.; Huang, J.-K.; Liu, K.-K.; Lee, Y.-H.; Liang, C.-T.; Chu, C.-W.; Li, L.-J. Wafer-Scale MoS_2 Thin Layers Prepared by MoO_3 Sulfurization. *Nanoscale* **2012**, *4*, 6637–6641.

38. Seo, J.; Jun, Y.; Park, S.; Nah, H.; Moon, T.; Park, B.; Kim, J.-G.; Kim, Y. J.; Cheon, J. Two-Dimensional Nanosheet Crystals. *Angew. Chem., Int. Ed.* **2007**, *46*, 8828–8831.

39. Li, H.; Lu, G.; Wang, Y.; Yin, Z.; Cong, C.; He, Q.; Wang, L.; Ding, F.; Yu, T.; Zhang, H. Mechanical Exfoliation and Characterization of Single- and Few-Layer Nanosheets of WSe_2, TaS_2, and $TaSe_2$. *Small* **2013**, *9*, 1974–1981.

40. Mead, D. G.; Irwin, J. C. Long Wavelength Optic Phonons in WSe_2. *Can. J. Phys.* **1977**, *55*, 379–382.

41. Sourisseau, C.; Cruege, F.; Fouassier, M.; Alba, M. Second-Order Raman Effects, Inelastic Neutron Scattering and Lattice Dynamics in 2H-WS_2. *Chem. Phys.* **1991**, *150*, 281–293.

42. Frey, G. L.; Tenne, R.; Matthews, M. J.; Dresselhaus, M. S.; Dresselhaus, G. Raman and Resonance Raman Investigation of MoS_2 Nanoparticles. *Phys. Rev. B* **1999**, *60*, 2883–2892.

43. Sekine, T.; Izumi, M.; Nakashizu, T.; Uchinokura, K.; Matsuura, E. Raman Scattering and Infrared Reflectance in 2H-$MoSe_2$. *J. Phys. Soc. Jpn.* **1980**, *49*, 1069–1077.

44. Lee, C.; Yan, H.; Brus, L. E.; Heinz, T. F.; Hone, J.; Ryu, S. Anomalous Lattice Vibrations of Single- and Few-Layer MoS_2. *ACS Nano* **2010**, *4*, 2695–2700.

45. Zhao, W.; Ghorannevis, Z.; Chu, L.; Toh, M.; Kloc, C.; Tan, P.-H.; Eda, G. Evolution of Electronic Structure in Atomically Thin Sheets of WS_2 and WSe_2. *ACS Nano* **2013**, *7*, 791–797.

46. Beal, A. R.; Knights, J. C.; Liang, W. Y. Transmission Spectra of Some Transition Metal Dichalcogenides. II. Group VIA: Trigonal Prismatic Coordination. *J. Phys. C: Solid State Phys.* **1972**, *5*, 3540.

47. Bromley, R. A.; Murray, R. B.; Yoffe, A. D. The Band Structures of Some Transition Metal Dichalcogenides. III. Group

VIA: Trigonal Prism Materials. *J. Phys. C: Solid State Phys.* **1972**, *5*, 759.

48. Kuc, A.; Zibouche, N.; Heine, T. Influence of Quantum Confinement on the Electronic Structure of the Transition Metal Sulfide TS$_2$. *Phys. Rev. B* **2011**, *83*, 245213-1-4.

49. Jiang, H. Electronic Band Structures of Molybdenum and Tungsten Dichalcogenides by the GW Approach. *J. Phys. Chem. C* **2012**, *116*, 7664–7671.

50. Zeng, H.; Liu, G.-B.; Dai, J.; Yan, Y.; Zhu, B.; He, R.; Xie, L.; Xu, S.; Chen, X.; Yao, W.; *et al*. Optical Signature of Symmetry Variations and Spin-Valley Coupling in Atomically Thin Tungsten Dichalcogenides. *Sci. Rep.* **2013**, *3*, 1608-1-5.

51. Salitra, G.; Hodes, G.; Klein, E.; Tenne, R. Highly Oriented WSe$_2$ Thin Films Prepared by Selenization of Evaporated WO$_3$. *Thin Solid Films* **1994**, *245*, 180–185.

52. Schellenberger, A.; Schlaf, R.; Mayer, T.; Holub-Krappe, E.; Pettenkofer, C.; Jaegermann, W.; Ditzinger, U. A.; Neddermeyeret, H. Na Adsorption on the Layered Semiconductors SnS$_2$ and WSe$_2$. *Surf. Sci.* **1991**, *241*, L25–L29.

53. Hulliger, F. In *Structural Chemistry of the Layer-Type Phases*; Lévy, F., Ed.; Reidel: Dordrecht, The Netherlands, 1976.

54. Xia, J.; Chen, F.; Li, J.; Tao, N. Measurement of the Quantum Capacitance of Graphene. *Nat. Nanotechnol.* **2009**, *4*, 505–509.